Smart Structures and Systems, *Vol. 18, No. 2 (2016) 197-216*
DOI: http://dx.doi.org/10.12989/sss.2016.18.2.197

Cone penetrometer incorporated with dynamic cone penetration method for investigation of track substructures

Won-Taek Hong[1a], Yong-Hoon Byun[2b], Sang Yeob Kim[1c] and Jong-Sub Lee[*1]

[1]*School of Civil, Environmental and Architectural Engineering, Korea University, 145 Anam-ro, Seongbuk-gu, Seoul 136-713, Republic of Korea*
[2]*Department of Civil and Environmental Engineering, University of Illinois at Urbana-Champaign, 205 North Mathews Ave., Urbana, IL 61801-2352, USA*

(Received July 13, 2015, Revised February 15, 2016, Accepted February 17, 2016)

Abstract. The increased speed of a train causes increased loads that act on the track substructures. To ensure the safety of the track substructures, proper maintenance and repair are necessary based on an accurate characterization of strength and stiffness. The objective of this study is to develop and apply a cone penetrometer incorporated with the dynamic cone penetration method (CPD) for investigating track substructures. The CPD consists of an outer rod for dynamic penetration in the ballast layer and an inner rod with load cells for static penetration in the subgrade. Additionally, an energy-monitoring module composed of strain gauges and an accelerometer is connected to the head of the outer rod to measure the dynamic responses during the dynamic penetration. Moreover, eight strain gauges are installed in the load cells for static penetration to measure the cone tip resistance and the friction resistance during static penetration. To investigate the applicability of the developed CPD, laboratory and field tests are performed. The results of the CPD tests, i.e., profiles of the corrected dynamic cone penetration index (CDI), profiles of the cone tip and friction resistances, and the friction ratio are obtained at high resolution. Moreover, the maximum shear modulus of the subgrade is estimated using the relationships between the static penetration resistances and the maximum shear modulus obtained from the laboratory tests. This study suggests that the CPD test may be a useful method for the characterization of track substructures.

Keywords: dynamic penetration; shear modulus; static penetration; track substructures; transferred energy

1. Introduction

Railway transport speed has been actively increasing due to the advances in railway technology. Moreover, in countries with developed railway technology, high-speed railway transport is the most commonly used type of public transportation (Chebli *et al*. 2008). However, increased train speed causes excessive lateral pressure and increased starting force and braking force to be applied to conventional lines. These problems can lead to changes in the condition of track substructures

*Corresponding author, Professor, E-mail: jongsub@korea.ac.kr
[a] Ph.D. Candidate, E-mail: 01698788767@korea.ac.kr
[b] Postdoctoral Fellow, E-mail: yhbyun@illinois.edu
[c] Ph.D. Student, E-mail: s3778@korea.ac.kr

http://www.techno-press.org/?journal=sss&subpage=8 ISSN: 1738-1584 (Print), 1738-1991 (Online)

and shear failure of the subgrade. Furthermore, deterioration of the ballast causes the destruction of ties and rails, leading to possible train derailment due to the loss of shock absorption and friction resistance (Clark *et al.* 2002). Thus, proper maintenance based on an accurate evaluation of the track substructures is required. To evaluate the condition of the track substructures including the ballast and subgrade, the test pit excavation method has been commonly used. The test pit excavation method has an advantage of directly evaluating the track substructures in situ conditions. However, because the test pit excavation method is a time-consuming and destructive method, it inevitably interrupts running time of the trains for long periods (Gallagher *et al*. 1999, Hugenschmidt 2000).

Non-destructive methods, such as ground penetrating radar (GPR) and the surface wave, have also been applied for track substructures investigation. Al-Qadi *et al*. (2010) applied GPR to the track substructures to detect the ballast fouling depth. While the GPR is cost-effective and explores large areas within a short time (Carpenter *et al*. 2004), it is difficult for it to profile the strength and stiffness along the depth. The surface wave method is also applied to railway track substructures (Anbazhagan *et al.* 2011, Vo *et al.* 2015); however, the surface wave method has not reached the practical application stage. For the compaction control of the subgrade during railway construction, studies on the light falling weight deflectometer (LFWD) and plate bearing test (PBT) have been applied (Correia *et al*. 2009). The LFWD and PBT may directly estimate the stiffness and deflection of the subgrade, but the ties and ballast should be removed for the application of these two methods in operating railway track substructures due to the limitation of the application range of the devices. Thus, a study on the in situ penetration test, which can directly characterize the track substructures along the depth and present the reference values to the non-destructive testing methods, is required.

In situ penetration test methods include the standard penetration test (SPT), cone penetration test (CPT), flat plate dilatometer test (DMT), pressuremeter test (PMT), and vane shear test (VST). These in situ penetration test methods have been reviewed as the investigation methods for railway track substructures (McHenry and Rose 2012). However, the DMT and VST require a borehole to reach the subgrade because the blade and the vane used in the DMT and VST cannot directly penetrate into the ballast layer, and the PMT cannot be applied to the ballast layer due to the large void in the ballast layer. Moreover, the SPT is not suitable for the ballast layer because the depth of the ballast layer under the tie is insufficient. Among the in situ penetration test methods, the studies on the application of the CPT to railway track substructures are most actively carried out. Note that the in-situ CPT usage continuously increases for common ground investigations because CPT does not require a borehole and gives reliable data (Lunne *et al.* 1997). However, the cone penetrometer used in CPT has a diameter of 35.7 mm (area = 10 cm^2), which significantly disturbs the track substructures. Furthermore, access for the normal penetrating rig used in CPT on the railway is not easy due to the large volume and weight of the rig. To apply CPT to railway track substructures, a modified penetrating rig, which can be operated on the railway, has been developed (McHenry and Rose 2012). However, the access route and application range of the rig are limited and the disturbance problem has not yet been resolved. To minimize the disturbance to the ground, studies on cone penetrometers with various diameters were conducted (Yoon and Lee 2012). Particularly, Byun *et al*. (2013) developed and applied a cone penetrometer with a helical type outer rod (CPH) to the track substructures. However, the rotation of the helical type outer rod was difficult due to the large friction resistance between the outer rod and the ballast. Moreover, the CPH only passes through the ballast without characterization of the ballast layer.

In this study, a cone penetrometer incorporated with the dynamic cone penetration method

(CPD) is developed, which evaluates the ballast by using the dynamic penetration method and the subgrade by using the static penetration method. From the results of the investigation of the track substructures using the CPD, dynamic penetration resistances are obtained in the ballast, and static penetration resistances are obtained in the subgrade. As the dynamic penetration resistance, corrected dynamic cone penetration index (CDI) is obtained. As the static penetration resistances, the cone tip resistance and friction resistance are obtained. In addition, the static penetration resistances are correlated with the shear modulus in laboratory tests for the estimation of the shear modulus in the field. This paper shows the entire shape and functions of the CPD and documents the application tests of the CPD.

2. Cone penetrometer incorporated with dynamic cone penetration method (CPD)

The CPD consists of an outer rod for dynamic penetration into the ballast layer and an inner rod for static penetration into the subgrade below the ballast layer, as shown in Fig. 1. Moreover, load cells with a diameter of 20 mm are installed on the front end of the inner rod for measurements of the cone tip resistance (q_c) and friction resistance (f_s). The outer rod has a diameter of 24 mm and the inner rod has a diameter of 16 mm.

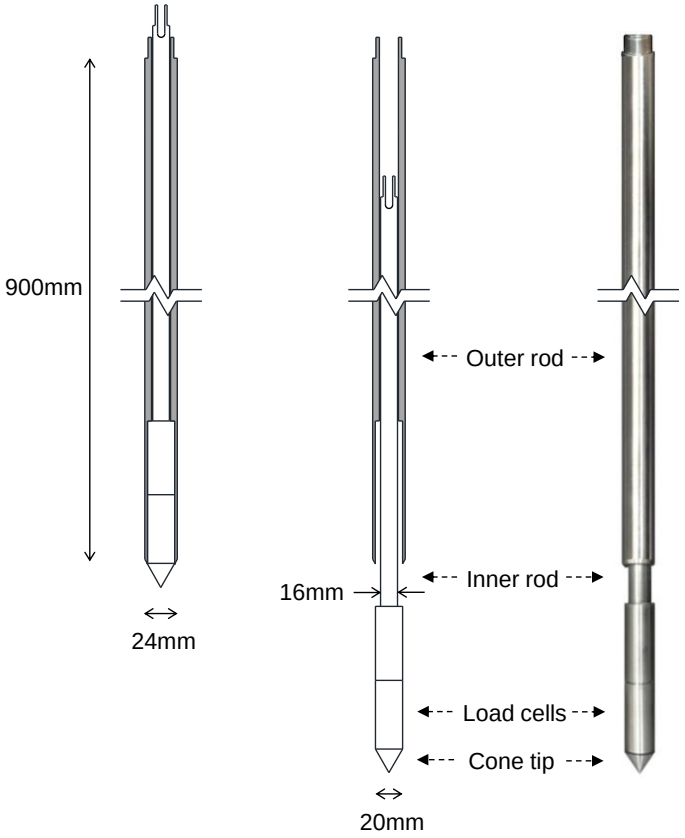

(a) Coupled (b) Uncoupled (c) Photographic image

Fig. 1 Cone penetrometer incorporated with the dynamic cone penetration method

2.1 Dynamic penetration

Dynamic penetration into the ballast layer is performed with a coupled form of the outer and inner rods (Fig. 1(a)). During the dynamic penetration, the penetration depth and dynamic responses are measured at each blow. The characteristics of the ballast layer can be obtained using the dynamic cone penetration index (DCPI), which is defined as follows (ASTM D6951)

$$DCPI_n[mm/blow] = P_n - P_{n-1} \tag{1}$$

where P_n and P_{n-1} denote the penetration depths (mm) at the n-th and n-1-th blows, respectively.

Before the dynamic penetration of the CPD, an energy-monitoring module (E-module) for measurements of the dynamic responses, a 78.5 N drop hammer and a guide are installed on the head of the CPD, as shown in Fig. 2. In the E-module, an accelerometer with a range of 10,000 g and electrical resistance type strain gauges connected as a full bridge are installed as the dynamic transducers.

Acceleration measured using the accelerometer is monitored through the data logger and a laptop. Moreover, force measured using the strain gauges is monitored through the bridge box, the data logger and the laptop. From the measured dynamic responses, the transferred energy (E) from the hammer to the head of the CPD can be calculated. In this study, the force-velocity integration method (ASTM D4633) is adopted for the calculation of transferred energy, as follows

$$E = \int F_{(strain)} \times V_{(acc)} dt \tag{2}$$

where $F_{(strain)}$ is the measured force, $V_{(acc)}$ is the calculated velocity from the measured acceleration, and t is the duration of the dynamic responses. The calculated transferred energy can be affected by the length of the outer rod and ground strength characteristics. In the case of the standard penetration test, Sancio and Bray (2005) reported that the rod length has little influence on the transferred energy calculated by using the force-velocity integration method when the N value is greater than 10. Because the outer rod length of the CPD is fixed at 900 mm and the subgrade and ballast layer are significantly compacted during the construction of railway track substructures, the effect of the rod length on the transferred energy may be negligible.

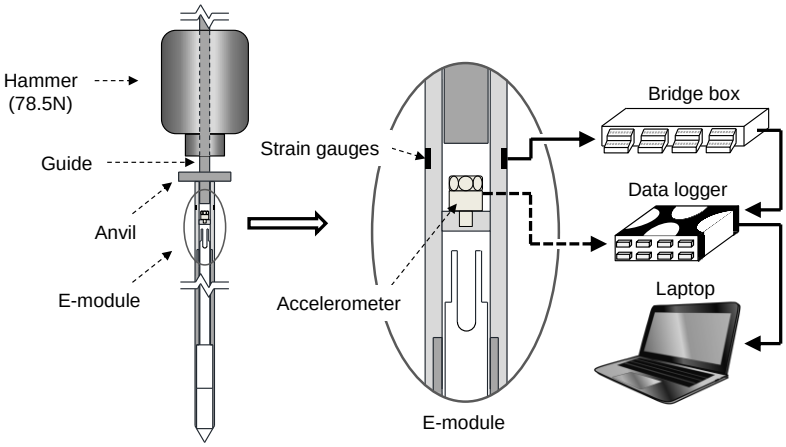

Fig. 2 Measurement system for the dynamic penetration

The operators and experimental conditions can affect the DCPI obtained from the dynamic penetration in the ballast layer. By correcting the DCPI using the transferred energy, more reliable results can be obtained. The n-th energy corrected dynamic cone penetration index from the transferred energy ($DCPI_{EC,\,n}$) is defined as

$$DCPI_{(EC,n)}[mm/blow] = DCPI_n \times \frac{E_{potential}}{E_n} \tag{3}$$

where $DCPI_n$ is the measured DCPI at the n-th blow, $E_{potential}$ is the potential energy of the drop hammer (45.13 N·m), and E_n is the energy transferred at the n-th blow. The calculation procedure of $DCPI_{EC}$ shows a result similar to the corrected N value corresponding to 60% of the theoretical maximum potential energy suggested by Seed *et al*. (1985) and Skempton (1986).

The dynamic cone penetration resistance can be affected not only by the users and the experimental conditions but also by the gravel constituting the ballast layer. The measured DCPI during the dynamic penetration of CPD can be affected by the position between the tip of CPD and the gravel. Thus, the irregularity in the DCPI profiles, which represent the condition of the ballast layer, may be corrected. To minimize the irregularity in the DCPI logs, the moving average is applied. The moving average is a way to represent an overall trend by averaging each value and the approximate values (Santamarina and Fratta 1998). In this study, the moving average is applied for each DCPI with a kernel of 3, with a higher weight factor in the center. The n-th dynamic cone penetration index, corrected by using the moving average, after energy correction ($DCPI_{EC,\,MA,\,n}$) is

$$DCPI_{(EC,MA,n)} = \frac{DCPI_{(EC,n-1)} + 2 \times DCPI_{(EC,n)} + DCPI_{(EC,n+1)}}{4} = CDI_n \tag{4}$$

where $DCPI_{(EC,\,n-1)}$, $DCPI_{(EC,\,n)}$, and $DCPI_{(EC,\,n+1)}$ denote the energy corrected DCPI at the n-1-th, n-th, and n+1-th blow, respectively. In this study, the dynamic cone penetration index corrected by using the transferred energy and the moving average ($DCPI_{EC,\,MA,\,n}$) is defined as CDI_n.

2.2 Static penetration

After the dynamic penetration of the CPD into the ballast layer, static penetration is carried out continuously in the subgrade. Before the static penetration, the E-module, hammer, and guide are removed from the head of the outer rod, the inner rod is extended, and the penetrator is installed. During the static penetration, the cone tip resistance and friction resistance are acquired. The load cells for static penetration consist of a load cell for the measurement of the cone tip resistance (q_c) and a load cell for the measurement of the friction resistance (f_s) as shown in Fig. 3. A cone tip with a diameter of 20 mm and an apex angle of 60˚ is connected at the end of the load cell for the cone tip resistance measurement. The area of the cone tip (D = 20 mm) is approximately 30% of the standard cone penetrometer (D = 35.7 mm). Furthermore, a friction sleeve with a diameter of 20 mm and a length of 50 mm is installed at the end of the load cell for friction resistance measurements. To measure the cone tip resistance and friction resistance separately, the load cells are separated at 0.5 mm intervals. The strain gauges are symmetrically installed on the wall for each load cell to minimize the influence of the eccentricity. Strain gauges consisting of two axes in the horizontal and vertical directions are used to compensate for the temperature effect (Yoon and Lee 2012).

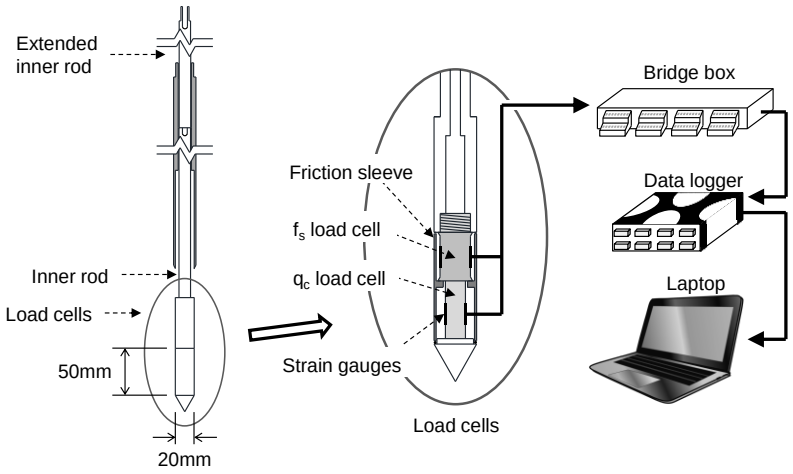

Fig. 3 Measurement system for the static penetration

During static penetration, the determination of the penetration rate is very important because the disturbance of the soil affects the static penetration resistances during the process (Bemben and Myers 1974, De Lima and Tumay 1991). Moreover, the penetration rate affects the drainage condition of the soil. Cho *et al*. (2004) noted the relationship between the drainage condition, the coefficient of consolidation, the cone tip shape, and the penetration rate as follows

$$\frac{t_{dis}}{t_{pen}} \approx \frac{d^2 \times v_{pen}}{\lambda \times c_v} \tag{5}$$

where t_{dis} is the timescale for pore pressure dissipation, t_{pen} is the timescale for penetration, d is the diameter of the cone penetrometer, v_{pen} is the penetration rate, λ is the length of the cone tip, and c_v is the coefficient of the consolidation. If t_{dis}/t_{pen} is greater than 1, the condition is regarded as undrained; if t_{dis}/t_{pen} is less than 1, the condition is regarded as drained. In this study, the penetration rate is determined as 1 mm/sec to perform the static penetration under the drained condition. At a penetration of 1 mm/sec, the cone tip resistance is the same as that at a penetration of 20 mm/sec and the friction resistance is slightly higher (Kim *et al.* 2008). Note that the penetration rate of 1 mm/sec is commonly adopted for micro-cones (Lee *et al*. 2009, Kim *et al*. 2010, Yoon *et al*. 2011).

As the cone size decreases, the cone tip resistance increases and the friction resistance decreases (De Lima and Tumay 1991, Lunne *et al.* 1997, Tumay *et al*. 1998). Therefore, considering the effects of the penetration rate and the cone size, the static penetration of the CPD produces slightly higher cone tip resistance and friction resistance than the standard in situ CPT. Note that both the cone tip resistance and friction resistance are measured at a sampling rate of 5 Hz. Thus, five points of the cone tip resistance and five points of friction resistance are obtained for each 1 mm.

2.3 Calibration of E-module and load cells

The loads acting on both the E-module during the dynamic penetration and the load cells during the static penetration cause changes to occur in the output voltage of the strain gauge circuits. Because the experimental results are obtained not as loads but as changes in output voltages, calibrations are performed to obtain the correlation factors between the loads and the output voltage in both the E-module and the load cells. The correlation factors are obtained by correlating the loads applied to the E-module and load cells with measured output voltage increments. Strain gauges installed on each of the load cells are connected in the form of a full bridge of the Wheatstone bridge; the relationship between the input voltage (V_{in}), output voltage (V_{out}), and strains applied to each of the strain gauges is

$$\frac{V_{out}}{V_{in}} = \frac{K}{4}\left(\varepsilon_1 - \varepsilon_2 + \varepsilon_3 - \varepsilon_4\right) \tag{6}$$

where K is the gauge factor, ε_1 and ε_3 are the strains installed in the vertical direction, and ε_2 and ε_4 are the strains installed in the horizontal direction. ε_1 and ε_3 are the strains caused by the loads and temperature changes, while ε_2 and ε_4 are the strains caused by the temperature and tension changes due to the applied load. From Eq. (6), the temperature effect can be compensated for, while the tension can be compensated for through the calibration. Thus, only the loads acting in the vertical direction can be obtained by converting the output voltages to loads using the correlation factors. The calibration results of the E-module and load cells for the measurements of cone tip resistance (q_c) and friction resistance (f_s) show good linearity, with a coefficient of determination (R^2) greater than 0.99. When 1.25 V is applied as the input voltage, the output voltages of the E-module and the load cells can be converted to loads using Eqs. (7)-(9).

$$F_{E\text{-}module}[kN] = 391.61 \times V_{out}[mV] \tag{7}$$

$$F_{qc}[kN] = 70.265 \times V_{out}[mV] \tag{8}$$

$$F_{fs}[kN] = 84.161 \times V_{out}[mV] \tag{9}$$

where, F is the force and the subscripts E-module, qc, and fs denote the energy monitoring module, cone tip resistance, and friction resistance, respectively. V_{out} is the output voltage corresponding to the force.

2.4 Experimental procedure

The investigation of the track substructures using the CPD is conducted as follows:

(1) A verticality guide of the CPD during the dynamic penetration is located on the adjacent ties, as shown in Fig. 4(a).
(2) The CPD is located on the guide; the E-module and a hammer guide with a 78.5 N hammer are connected to the CPD, and then dynamic penetration is performed, with a drop height of 575 mm, as shown in Fig. 4(b). Note that the weight and drop height of the hammer are the same as those specified in ASTM D6951. During the dynamic penetration, the blow number, penetration depth, and dynamic responses are measured.

(3) After completion of the dynamic penetration, the E-module, hammer and hammer guide are removed; the inner rod is extended while installing the penetrator, as shown in Fig. 4(c).
(4) Static penetration of the inner rod is performed, with a penetration rate of 1 mm/sec, as shown in Fig. 4(d). During the static penetration, the cone tip resistance and friction resistance are measured.

3. Application tests

3.1 Laboratory test

To test the applicability via a laboratory test, a parallel-piped chamber is used, the inner dimensions of which are 750 mm in length and width and 1,000 mm in height. To simulate the track substructures, the weathered soil is deposited with compaction using a hammer with a weight of 44.1 N and a drop height of 450 mm.

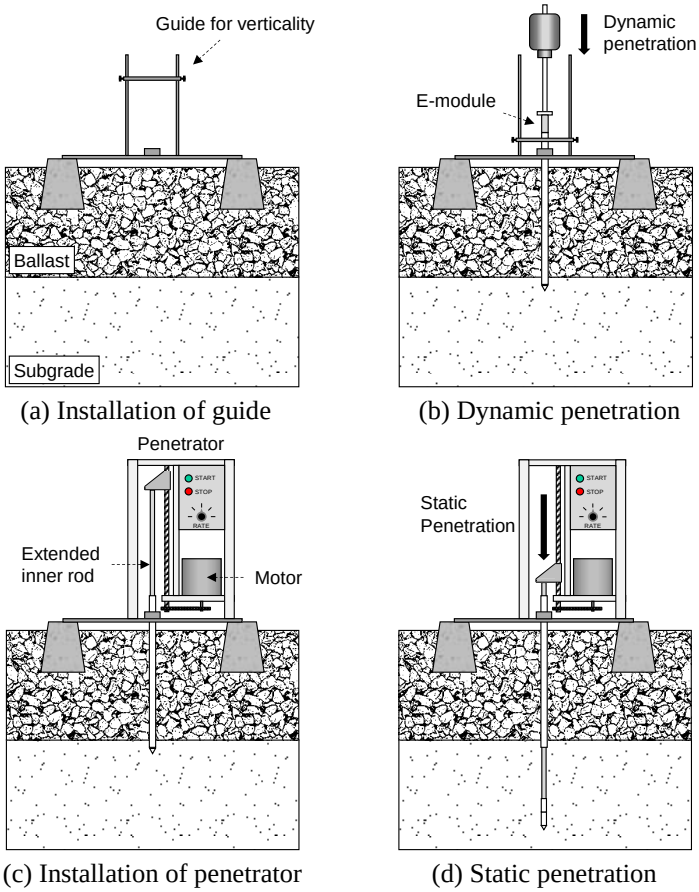

(a) Installation of guide (b) Dynamic penetration

(c) Installation of penetrator (d) Static penetration

Fig. 4 Experimental procedure

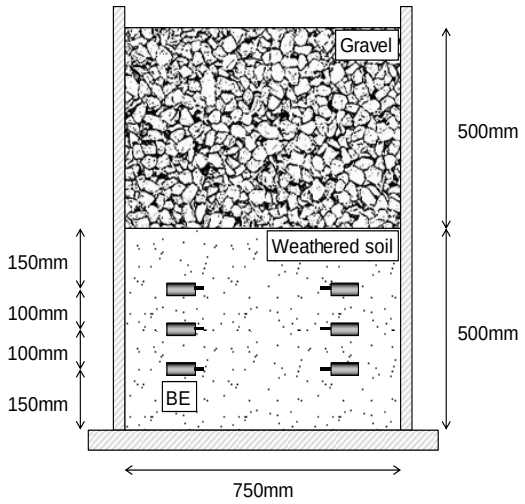

Fig. 5 Cross section of the chamber; BE denotes the bender element

Table 1 Index properties of weathered soil

Coefficient of Uniformity (C_u)	Coefficient of Curvature (C_g)	Specific Gravity (G_s)	Maximum Void Ratio (e_{max})	Minimum Void Ratio (e_{min})	USCS
10.94	1.16	2.65	0.78	0.42	SW

Table 2 Index properties of gravel

Coefficient of Uniformity (C_u)	Coefficient of Curvature (C_g)	Specific Gravity (G_s)	Content of soft fragment (%)	Abrasion rate (%)	USCS
1.63	1.09	2.62	1.9	21.5	GP

* content of soft fragment and abrasion rate are based on the weight

For the deposition of the compacted, weathered soil with a depth of 100 mm, 903.8 N of oven-dried weathered soil is used and the compaction is performed twice in 25 places. By repeating the compacting procedure five times, the compacted, weathered soil, with a thickness of 500 mm is deposited from the bottom of the chamber, as shown in Fig. 5.

The index properties of the used weathered soil are summarized in Table 1; the weathered soil is classified as a well graded sandy soil according to the unified soil classification system (USCS).

The unit weight and relative density of the deposited weathered soil are 16.1 kN/m^3 and 63%, respectively. During the deposition of the weathered soil, three pairs of bender elements are installed at heights of 150 mm, 250 mm, and 350 mm from the bottom, as shown in Fig. 5. Note that a bender element is a transducer that generates and receives shear waves in soil with a high-resolution (Lee and Santamarina 2005). Above the compacted weathered soil, gravel is

deposited to simulate the ballast layer using the same procedure adopted for the preparation of the compacted weathered soil. The index properties of the used gravel are summarized in Table 2.

In the laboratory test, the penetration tests are performed twice (L-1, L-2) for the simulated track substructures. As a procedure of the laboratory tests, the CPD dynamically penetrates into the simulated ballast layer while measuring the blow counts and penetration depths, and the responses of the strain gauges and the accelerometer are gathered to calculate the transferred energy. In the simulated ballast layer, corrected dynamic cone penetration index (CDI) profiles are obtained. When the tip of the CPD reaches the compacted weathered soil, shear waves are measured using the installed bender elements; the static penetration of the inner rod is then performed to measure the cone tip resistance and the friction resistance in the compacted weathered soil. Additionally, the relationships between the static penetration resistances (the cone tip resistance and the friction resistance) and the shear wave velocity are derived.

To obtain the additional relationship between the static penetration resistances and shear wave velocities, a compacted specimen composed of only weathered soil with a depth of 1,000 mm is prepared. In the weathered soil specimen, four pairs of bender elements are installed at heights of 200 mm, 400 mm, 600 mm, and 800 mm from the bottom and a static penetration test is conducted to measure the cone tip resistance and friction resistance.

3.2 Field test

To apply the CPD to the field, a railway located in Seoul is selected as a target spot. The target railway has a cross section of the common track substructures, including a ballast layer with a depth of 400~500 mm and a subgrade layer. In the field test, by applying the CPD to the track substructures that were actually built and used, the applicability of the CPD is verified. The penetration tests for the target spot are performed at two points (F-1 and F-2), whose separation distance is approximately 3.6 m.

4. Experimental results and analyses

In the laboratory tests (L-1 and L-2), the dynamic responses, blow counts and penetration depths are measured during the dynamic penetration into the gravel layer. The cone tip resistance and friction resistance are measured in the weathered soil with the shear wave acquisition during the static penetration. Similarly, in the field test (F-1 and F-2), dynamic responses, blow counts, and penetration depths are measured during the dynamic penetration into the ballast layer. The cone tip resistance and friction resistance are measured in the subgrade during the static penetration. Furthermore, the maximum shear modulus on the subgrade is estimated based on the derived relationship between the static penetration resistances and the shear wave velocity from the laboratory tests.

4.1 Dynamic penetration resistance

The energy transferred from the drop hammer to the E-module is calculated to compute the energy corrected dynamic cone penetration index. The calculation process of the transferred energy, using the dynamic responses measured at a depth of 383 mm in L-1 and a depth of 278 mm in F-1, is plotted in Fig. 6.

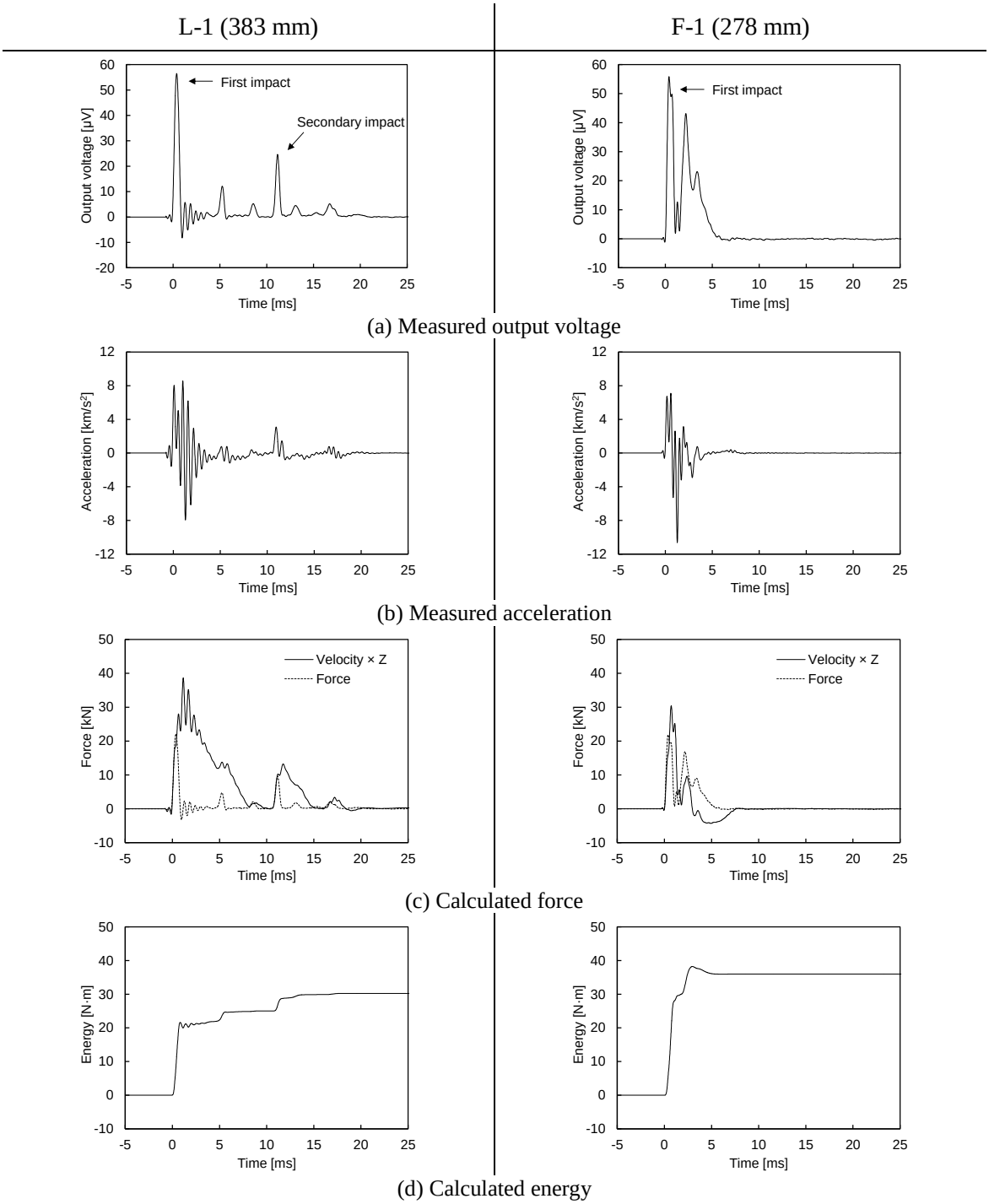

(a) Measured output voltage

(b) Measured acceleration

(c) Calculated force

(d) Calculated energy

Fig. 6 Calculation process of the transferred energy

Fig. 6(a) shows the output voltage measured using the strain gauges. In the case of L-1 (383 mm), the output voltage dramatically increases due to the impact of the hammer at approximately 0 ms, and a change in output voltage due to the secondary impact of the hammer is measured at approximately 11 ms. In the case of F-1 (278 mm), the first change in output voltage due to the impact of the hammer occurs at approximately 0 ms; this positive output voltage continues to approximately 6 ms due to not only the transmitted wave but also the influence of the longitudinal wave reflected from the ballast. Fig. 6(b) shows the measured acceleration using the accelerometer. The dotted line in Fig. 6(c) shows the converted force calculated by multiplying the impedance (Z) of the E-module by the velocity, which is integrated from the acceleration. In the case of L-1 (383 mm), the velocity of the CPD rapidly increases due to the hammer blow at 0 ms and then becomes zero; the velocity increases again at 11 ms. The second increase in the force and the velocity comes from the re-contact of the drop hammer with the anvil, which is the secondary impact (Lee *et al*. 2010). The solid line in Fig. 6(c) represents the force calculated by multiplying the calibration factor by the output voltage (Fig. 6(a)) measured using the strain gauges (Eq. (7)).

The transferred energy calculated using the force and velocity via the F-V integration method (Eq. (2), ASTM D4633) is plotted in Fig. 6(d). The shapes of the transferred energy with time show different forms depending on the reaction force on the target ground. The case of L-1 (383 mm) shows the energy-time form of easy driving, such as a pile driven into soft ground. The case of F-1 (278 mm) shows the form of hard driving, such as a pile driven into stiff ground (Pile Dynamics Inc. 2000). The transferred energy values at L-1 (383 mm) and F-1 (278 mm) are calculated as being approximately 30.22 N·m and 38.23 N·m, respectively; the transferred energy in the case of F-1 (278 mm) is greater than that in the case of L-1 (383 mm) because the ballast layer of the field tests is denser than the ballast layer of the laboratory tests. The transferred energy profiles versus the penetration depth for the laboratory and field tests are plotted in Fig. 7. The potential energy of the hammer is approximately 45.13 N·m for both tests, which is indicated by the thick dotted lines in Fig. 7. The average values of the transferred energies of L-1 and F-1 are calculated as being approximately 28.81 N·m and 38.57 N·m, respectively.

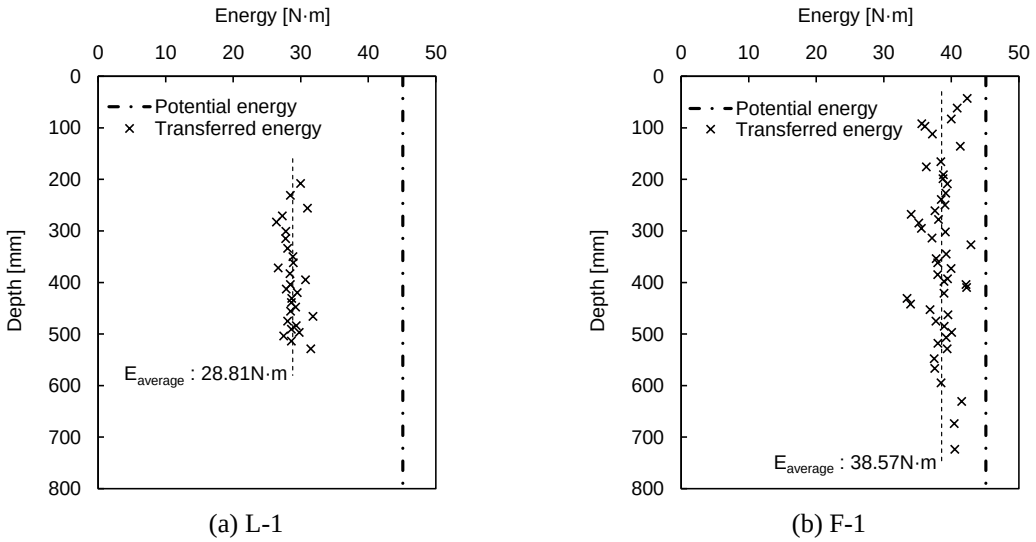

(a) L-1 (b) F-1

Fig. 7 Transferred energy

The CDI profiles, i.e., the corrected dynamic cone penetration index profiles, are shown in Fig. 8. The CDI measured in the laboratory tests (Fig. 8(a)) gradually decreased to 11~13 mm/blow with the penetration depth. Then, the CDI rapidly increased at the penetration depth of 500 mm, which is the interface between the ballast and the weathered soil. The CDI measured in the field test shows high values near the surface penetration due to the free stress effects; the CDI converges to 3~10 mm/blow at a depth of 200 mm. The CDI rapidly increases from the depths of 560 mm (F-1) and 440 mm (F-2), which are estimated as the interfaces between the ballast and the subgrade. The depth difference of the interface between F-1 and F-2 is expected as a result of the settlement of the track substructures around F-1; to compensate for this settlement, the ballast may be filled with gravel. Such difference in the depth of similar layers appears in the static penetration results.

4.2 Static penetration resistance

After dynamic penetration in the ballast, the static penetrations are performed continuously in the weathered soil (L-1 and L-2) and the subgrade (F-1 and F-2). The cone tip resistances and friction resistances are measured at every penetration depth, with increments of 0.2 mm. The experimental results of the laboratory test (L-1 and L-2) are plotted in Fig. 9. The cone tip resistances of L-1 and L-2 (Fig. 9(a)) rapidly increase with the start of static penetration due to the confining stress of the ballast; the resistances then converge to 6~8 MPa. The friction resistances of L-1 and L-2 (Fig. 9(b)) show a trend similar to that of the cone tip resistances and converge to 50~140 kPa. The friction ratio, which is the ratio of the friction resistance to the cone tip resistance, is calculated as being approximately 1%~2% (Fig. 9(c)). From the cone tip resistance, friction resistance and friction ratio, the weathered soil layer is categorized as silty sand to sandy silt (Lunne *et al*. 1997).

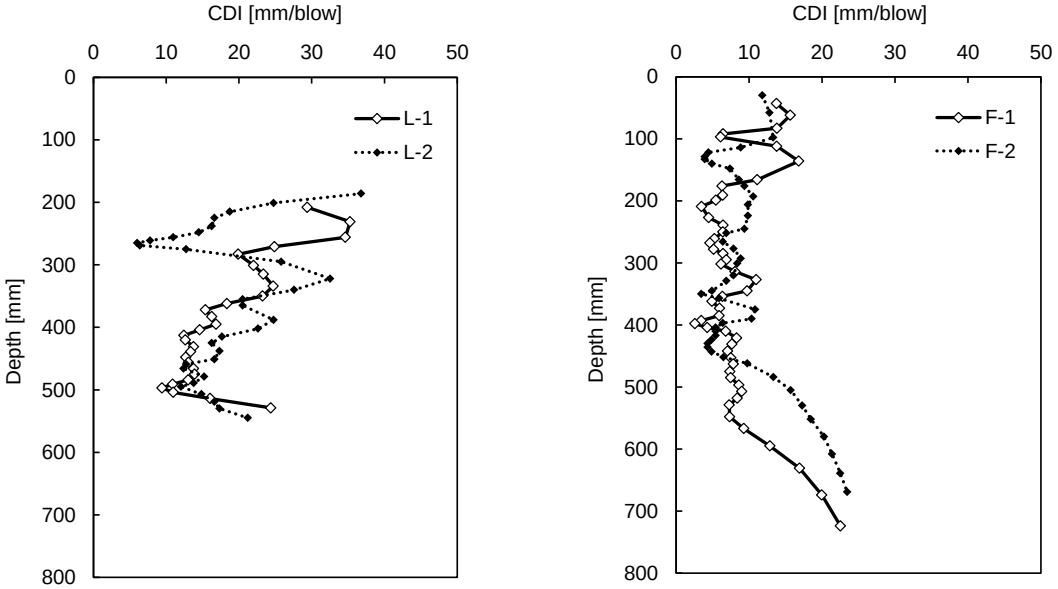

(a) Laboratory test (b) Field test

Fig. 8 Experimental results of the dynamic penetration

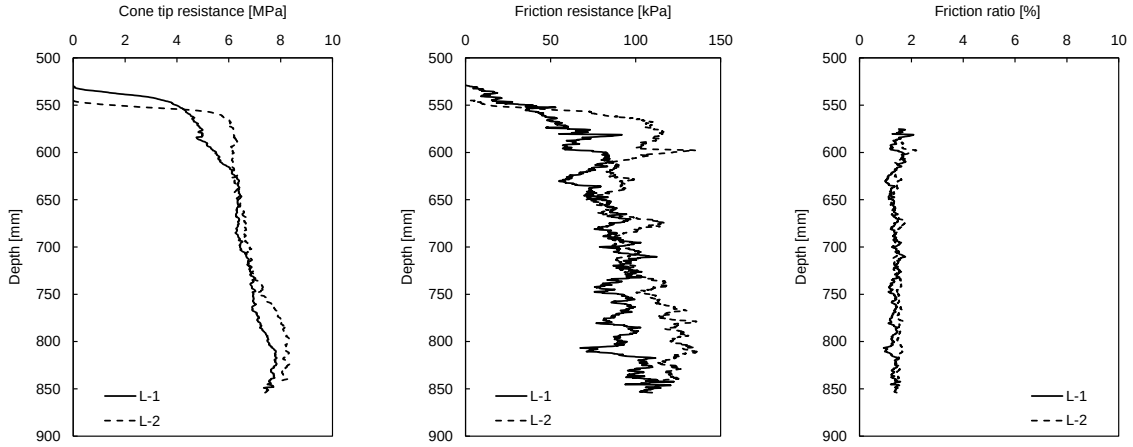

(a) Cone tip resistance (b) Friction resistance (c) Friction ratio

Fig. 9 Experimental results of the static penetration in the laboratory test

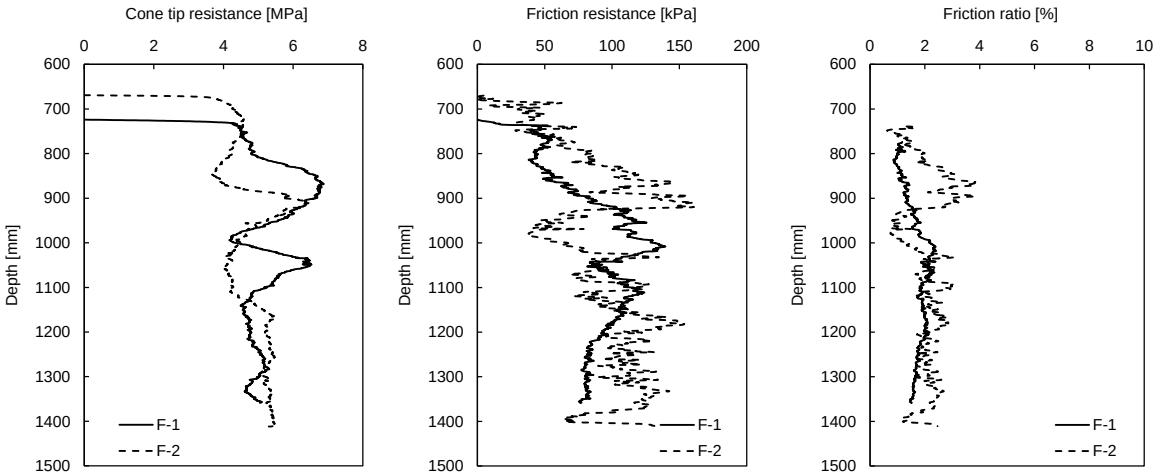

(a) Cone tip resistance (b) Friction resistance (c) Friction ratio

Fig. 10 Experimental results of the static penetration in the field test

The experimental results of the field tests (F-1 and F-2) are shown in Fig. 10. The total penetration depths of F-1 and F-2 are 1,359 mm and 1,412 mm from the tops of the ties, respectively. The cone tip resistances (Fig. 10(a)) are measured at approximately 4~7 MPa, while the friction resistances (Fig. 10(b)) are measured at approximately 50~150 kPa. Additionally, the friction ratio (Fig. 10(c)) is calculated as approximately 1%~3%, representing the behavior of silty sand to sandy silt and sandy silt to clayey silt (Lunne *et al*. 1997).

The CDI and the cone tip resistance profiles of F-1 and the F-2 show a trend similar to a gap in the penetration depth, as shown in Figs. 8(b) and 10(a). For example, Fig. 8(b) shows that the CDI of F-1 rapidly increases at a depth of 560 mm and the CDI of F-2 rapidly increases at a depth of

440 mm. Moreover, Fig. 10(a) shows that the second peak cone tip resistance of F-1 appears at an approximate depth of 1,040 mm and the second peak cone tip resistance of F-2 appears at an approximate depth of 910 mm. To estimate the gap in the penetration depth, cross correlation is performed using the cone tip resistance profiles of F-1 and F-2. The cross correlation produces a depth difference of 131 mm. That is, the subgrade at F-1, which shows strength characteristics similar to those at F-2, is located 131 mm deeper than the F-2 point. Based on the cross correlation, the CDI profile (Fig. 8(b)) and cone tip resistance profile (Fig. 10(a)) obtained in F-1 are adjusted upward along the depth of 131 mm and compared with those of F-2, as shown in Fig. 11. The CDI (Fig. 11(a)) and the cone tip resistance profiles (Fig. 11(b)) are much more coherent in F-1 and F-2.

4.3 Shear modulus

Shear modulus significantly affects the behavior of the track substructures that support the repeating dynamic load of the train. In this study, the relationships between the static penetration resistances and shear modulus are obtained from the laboratory tests to estimate the shear modulus in the field using the static penetration resistances. The correlations between the static penetration resistances and the shear wave velocity measured in the laboratory tests are plotted in Fig. 12. Fig. 12 shows that the shear wave velocity can be estimated using Eqs. (10) and (11).

$$V_s[m/s] = 82 \times q_c^{0.24}[MPa] \tag{10}$$

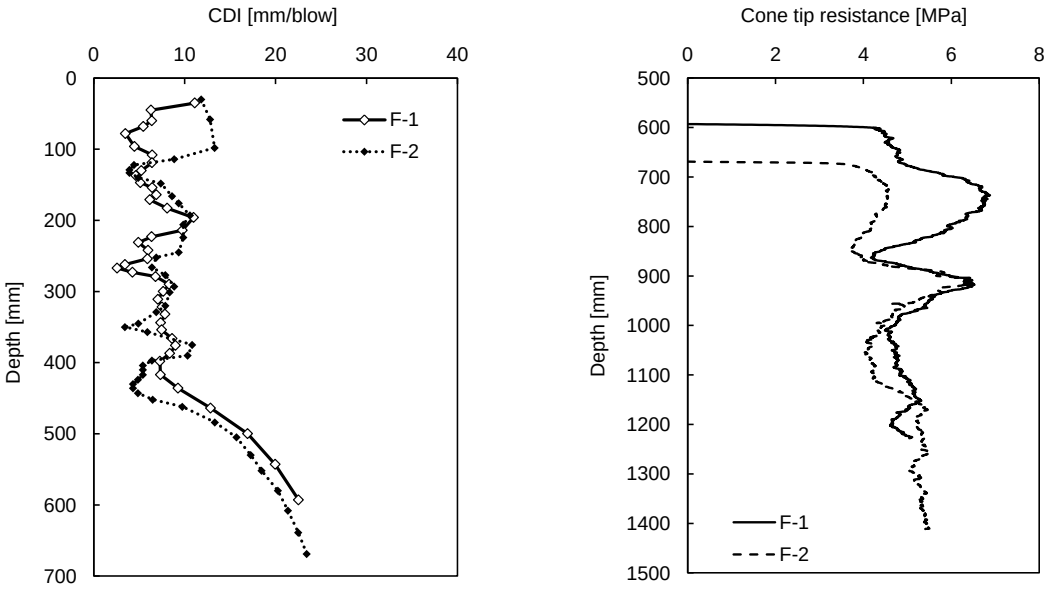

(a) CDI (b) Cone tip resistance

Fig. 11 Corrected field logs according to the result of cross correlation

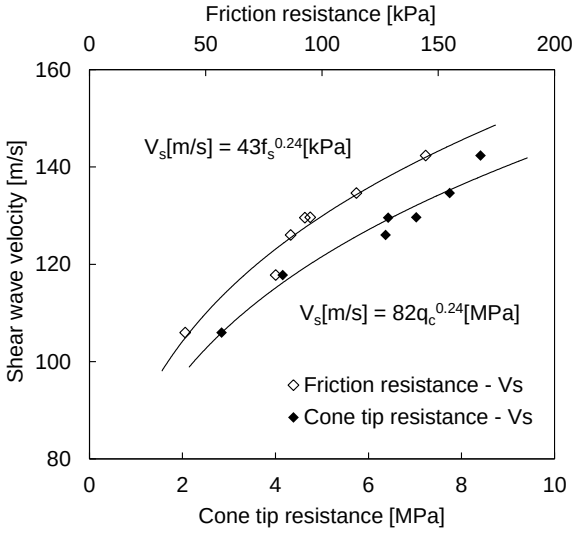

Fig. 12 Estimation of the shear wave velocity using static penetration resistances

$$V_s[m/s] = 43 \times f_s^{0.24}[kPa] \tag{11}$$

where V_s is the shear wave velocity and q_c and f_s are the cone tip resistance and friction resistance, respectively.

By using the shear wave velocity, the maximum shear modulus can be calculated as follows

$$G_{max} = \rho \times V_s^2 \tag{12}$$

where G_{max} is the maximum shear modulus in a low strain and ρ and V_s are the mass density and shear wave velocity measured in the laboratory test, respectively.

The relationships between the static penetration resistances and the maximum shear modulus calculated from Eq. (12) are plotted in Fig. 13. From Fig. 13, the maximum shear moduli, estimated using the experimental results of CPD, are

$$G_{max}[MPa] = 11.7 \times q_c^{0.48}[MPa] \tag{13}$$

$$G_{max}[MPa] = 3.2 \times f_s^{0.48}[kPa] \tag{14}$$

The G_{max} profiles estimated for the F-1 and F-2 tests using Eqs. (13) and (14) are plotted in Fig. 14. The G_{max} of both F-1 and F-2 is estimated at approximately 20~35 MPa along the penetration depths in the subgrade layer. Because Eqs. (13) and (14) are derived based on the shear wave velocity measured in the newly deposited specimen, the estimated G_{max} may be considered as the minimum value of G_{max} in the F-1 and F-2 sites.

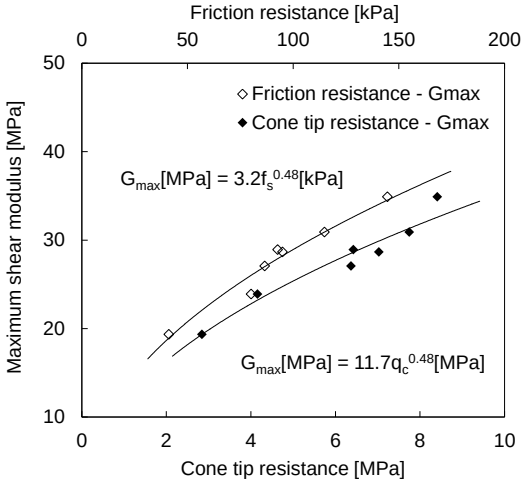

Fig. 13 Estimation of the maximum shear modulus using static penetration resistances

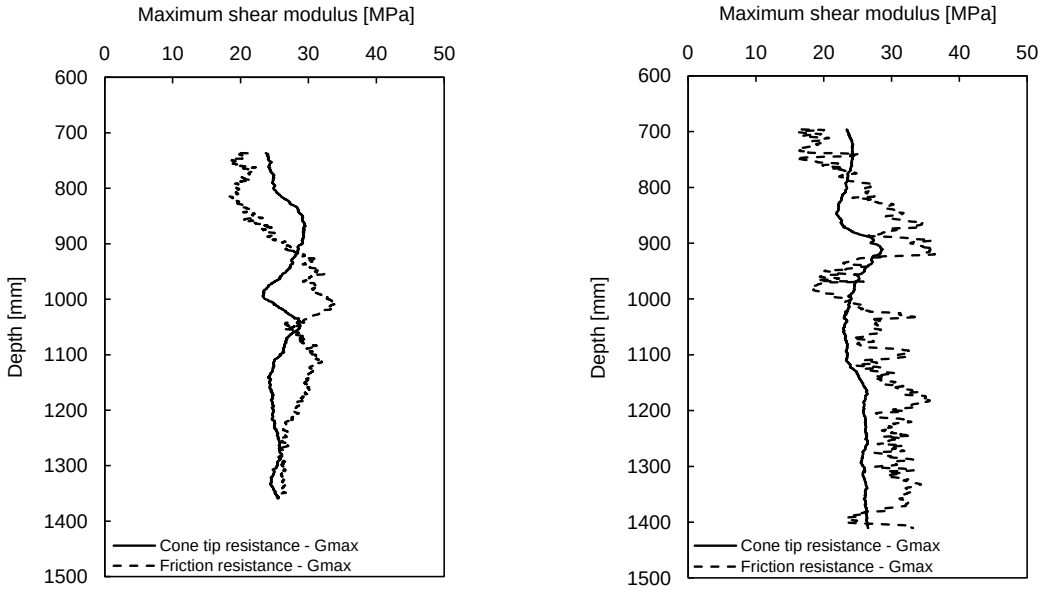

(a) F-1 (b) F-2

Fig. 14 Estimated maximum shear modulus in the field

5. Conclusions

In this study, a cone penetrometer incorporated with the dynamic cone penetration method (CPD) is developed to investigate track substructures. The CPD consists of an outer rod with a diameter of 24 mm and an inner rod with a diameter of 16 mm. At the end of the inner rod, load

cells for measuring the cone tip and friction resistances are installed. In the ballast layer, the CPD dynamically penetrates with a coupled form of the outer and inner rods. After the dynamic penetration in the ballast layer, static penetration is carried out continuously into the subgrade with an uncoupled form of the outer and inner rods. To measure the dynamic responses during the dynamic penetration of the CPD, an E-module is connected to the head of the CPD and a 78.5 N drop hammer and guide are installed on top of the E-module.

As the application tests of the CPD, two laboratory tests (L-1 and L-2) and two field tests (F-1 and F-2) are performed. A simulated track substructure is prepared for laboratory tests, and a railway located in Seoul, Korea is selected for field tests. In both laboratory and field tests during the dynamic penetration in the ballast layer, penetration depths and blow counts are recorded and the dynamic responses of the E-module are measured at each blow to compute the energy transferred from the hammer to E-module. Then, the corrected dynamic cone penetration index (CDI), which is corrected using the transferred energy and moving average, is obtained. During the static penetration in the laboratory tests, static penetration resistances and the shear waves are measured to obtain the relationship between the static penetration resistances and shear modulus to estimate the shear modulus in the field.

The experimental results of the laboratory tests show that the CDI in the simulated ballast layer decreases as the penetration depth increases and clearly detects the interface between the simulated ballast layer and the weathered soil. The static penetration resistances measured in the weathered soil gradually increase along the penetration depth. Moreover, from the cone tip and friction resistances measured during the static penetration, the weathered soil is classified as silty sand to sandy silt. In the case of field tests, the CDI in the ballast layer is smaller than that in the laboratory tests due to the hardening effect of the train and the fouling effect. However, the CDI in both laboratory and field tests clearly detects the interface between the ballast layer and subgrade layer at depths of approximately 440~560 mm. Furthermore, the maximum shear modulus of the subgrade is estimated as being 20~35 MPa. The cross correlation of the cone tip resistances detected in the field produces a depth difference at two locations, which may result from the filling of gravel into the ballast layer to compensate for the settlement.

Because the CPD developed in this study can characterize the ballast layer via dynamic penetration and the subgrade layer via static penetration, the CPD may be a useful device for investigating track substructures.

Acknowledgments

This research was supported by a grant (16RTRP-B067919-04) from Railroad Technology Research Program funded by Ministry of Land, Infrastructure and Transport of Korean government.

References

Al-Qadi, I.L., Xie, W., Roberts, R. and Leng, Z. (2010), "Data analysis techniques for GPR used for assessing railroad ballast in high radio-frequency environment", *J. Transportation Eng. - ASCE*, **136**(4), 392-399.

Anbazhagan, P., Lijun, S., Buddihima, I. and Cholachat, R. (2011), "Model track studies on fouled ballast

using ground penetrating radar and multichannel analysis of surface wave", *J. Appl. Geophys.*, **74**, 175-184.
ASTM D4633 (2005), "Standard test method for energy measurement for dynamic penetrometers", *Annual Book of ASTM Standard*, **04.08**, ASTM International, West Conshohocken, PA.
ASTM D6951 (2009), "Standard test method for use of the dynamic cone penetrometer in shallow pavement applications", *Annual Book of ASTM Standard*, **04.03**, ASTM International, West Conshohocken, PA.
Bemben, S.M. and Myers, H.J. (1974), "The influence of rate of penetration on static cone resistance in connecticut river valley varved clay", *Proceedings of the European Symposium on Penetration Testing*, Stockholm, 33-34.
Byun, Y.H., Kim, J.H. and Lee, J.S. (2013), "Cone penetrometer with a helical-type outer screw rod for evaluation of the subgrade condition", *J. Transportation Eng. - ASCE*, **139**, 115-122.
Carpenter, D., Jackson, P.J. and Jay, A. (2004), "Enhancement of the GPR method of railway trackbed investigation by the installation of radar detectable geosynthetics", *NDT & E Int.*, **37**, 95-103.
Chebli, H., Clouteau, D. and Schmitt, L. (2008), "Dynamic response of high-speed ballasted railway tracks: 3D periodic model and in situ measurements", *Soil Dyn. Earthq. Eng.*, **28**, 118-131.
Cho, G.C., Lee, J.S. and Santamarina, J.C. (2004), "Spatial variability in soils: High resolution assessment with electrical needle probe", *J. Geotech. Geoenviron.*, **130**(8), 843-850.
Clark, M., McCann, D.M. and Forde, M.C. (2002), "Infrared thermographic investigation of railway track ballast", *NDT & E Int.*, **35**, 83-94.
Correia, A.G., Martins, J., Caldeira, L., Neves, D., Maranha, E. and Delgado, J. (2009), "Comparison of in situ performance-based tests methods to evaluate moduli of railway embankments", In *Bearing Capacity of Roads, Railways and Airfields. 8th International Conference*, IL, 1331-1340.
De Lima, D.C. and Tumay, M.T. (1991), "Scale effects in cone penetration tests", *Proceedings of the Geotechnical Engineering Congress*, Boulder, Colorado.
Gallagher, G.P., Leiper, Q., Wiliamson, R., Clark, M.R. and Forde, M.C. (1999), "The application of time domain ground penetrating radar to evaluate railway track ballast", *NDT & E Int*., **32**, 463-468.
Hugenschmidt, J. (2000), "Railway track inspection using GPR", *J. Appl. Geophys.*, **43**, 147-155.
Kim, K., Prezzi, M., Salgado, R. and Lee, W. (2008), "Effect of Penetration rate on cone penetration resistance in saturated clayey soils", *J. Geotech. Geoenviron.*, **134**(8), 1142-1153.
Kim, R., Lee, W. and Lee, J.S. (2010), "Temperature-compensated cone penetration test mini-cone using fiber optic sensors", *Geotech. Test. J.*, **33**(3), 243-252.
Lee, C., Lee, J.S., An, S. and Lee, W. (2010), "Effect of secondary impacts on SPT rod energy and sampler penetration", *J. Geotech. Geoenviron.*, **136**(3), 522-526.
Lee, J.S. and Santamarina, J.C. (2005), "Bender element: Performance and signal interpretation", *J. Geotech. Geoenviron.*, **131**(9), 1063-1070.
Lee, W., Shin, D.H., Yoon, H.K. and Lee, J.S. (2009), "Micro-cone penetrometer for more concise subsurface layer detection", *Geotech. Testing Journal*, ASTM, **32**(4), 358-364.
Lunne, T., Robertson, P.K. and Powell, J.J.M. (1997), *Cone penetration testing in geotechnical practice*, Blackie Academic & Professional, London, 352.
McHenry, M.T. and Rose, J.G. (2012), *Railroad subgrade support and performance indicators: a review of available laboratory and in-situ testing methods*, Department of Civil Engineering and Kentucky Transportation Center, University of Kentucky, KY, 39.
Pile Dynamics Inc. (2000), *PDA-W Users manual*, OH.
Sancio, R.B. and Bray, J. (2005). "An assessment of the effect of rod length on SPT energy calculations based on measured field data", *Geotech. Testing Journal*, ASTM, **28**(1), 1-9.
Santamarina, J.C. and Fratta, D. (1998), *Introduction to discrete signals and inverse problems in civil Engineering*, ASCE Press, Virginia, 327.
Seed, H.B., Tokimatsu, K., Harder, L.F. and Chung, R.M. (1985), "Influence of SPT procedures in soil liquefaction resistance evaluation", *J. Geotech. Eng.*, **111**(12), 1425-1445.
Skempton, A.W. (1986), "Standard penetration test procedures and the effects in sands of overburden pressure, relative density, particle size, ageing and overconsolidation", *Geotechnique*, **36**(3), 425-447.

Tumay, M.T., Kurup, P.U. and Boggess, R.L. (1998), "A continuous intrusion electronic miniature cone penetration test (CIM-CPT) system for site characterization", *Proceedings of the International Conference on Site Characterization 98*, Atlanta, GA.

Vo, P.T., Ngo, H.H., Guo, W., Zhou, J.L., Listowski, A., Du, B., Wei, Q. and Bui, X. T. (2015), "Stormwater quality management in rail transportation - Past, present and future", *Sci. Total Environ.*, **512-513**, 353-363.

Yoon, H.K., Jung, S.H. and Lee, J.S. (2011), "Characterization of subsurface spatial variability by cone resistivity penetrometer", *Soil Dyn. Earthq. Eng.*, **31**(7), 1064-1071.

Yoon, H.K. and Lee, J.S. (2012), "Microcones configured with full-bridge circuits", *Soil Dyn. Earthq. Eng.*, **41**, 119-127.

CC